The PIDDosome controls cardiomyocyte polyploidization during postnatal heart development

Leone M[1], Kinz N[1], Eichin F[1], Obwegs D[1], Sladky VC[1], Rizzotto D[2], Manzl C[3], Moos K[4], Jacotot ED[5,6], Savko C[7], Sussman MA[7], Boerries M[4,8], Villunger A[1,2*]

[1]Institute for Developmental Immunology, Biocenter, Medical University of Innsbruck, Innsbruck, Austria
[2]CeMM Research Center for Molecular Medicine of the Austrian Academy of Sciences, 1090 Vienna, Austria
[3]Institute of Pathology, Neuropathology and Molecular Pathology, Medical University of Innsbruck, 6020 Innsbruck, Austria
[4] Institute of Medical Bioinformatics and Systems Medicine (IBSM), Medical Center – University of Freiburg, Faculty of Medicine, University of Freiburg, Breisacher Strasse 153, 79110 Freiburg, Germany
[5]Inserm U1268, Medicinal Chemistry and Translational Research. Paris, F-75006, France
[6]Faculté de Pharmacie, UMR 8038 CiTCoM, Université Paris Cité, Paris, F-75006, France
[7]San Diego State University Heart Institute and Department of Biology, San Diego State University, 5500 Campanile Drive, San Diego, CA 92182, USA.
[8] German Cancer Consortium (DKTK), Partner site Freiburg, a partnership between DKFZ and Medical Center - University of Freiburg, Hugstetter Strasse 55, 79106 Freiburg, Germany

Running Title: The PIDDosome controls cardiomyocyte ploidy

Correspondence:
Prof. Andreas Villunger, PhD
Institute for Developmental Immunology
Biocenter, Medical University of Innsbruck
Innrain 80, A-6020, Innsbruck, AT
Ph: +43-512-9003-70380
Fax: +43-512-9003-73960
Email: andreas.villunger@i-med.ac.at
ORCID: 0000-0001-8259-4153

Marina Leone, PhD
Institute for Developmental Immunology
Biocenter, Medical University of Innsbruck
Innrain 80, A-6020, Innsbruck, AT
Ph: +43 (0)512-9003-70982
Fax: +43 (0)512-9003-70982
Email: macileo@gmail.com
ORCID: 0000-0001-6839-6265

Abstract

The mammalian adult heart is a post-mitotic organ characterized by mainly polyploid cardiomyocytes (CMs). The post-mitotic status of polyploid adult CMs poses a clear limit to heart regeneration. Thus, understanding how CMs acquire this polyploid status is relevant to heart regeneration therapies. Here, we aim to unveil that the PIDDosome, a multi-protein complex known to limit scheduled and accidental polyploidization events by activating p53, implements a CM-specific genetic program that controls polyploidization during postnatal heart development in mice. Flow cytometric DNA content analysis coupled with image-based 3D volumetric measurements of CM nuclei showed that PIDDosome knockout animals harbor significantly more polyploid CM nuclei compared to WT controls. Remarkably, the increased CM ploidy levels do not interfere with cardiac structure or functional output and is implemented in a cell-autonomous manner. During early heart development, ploidy analyses revealed that the PIDDosome starts to shape CM ploidy at postnatal day 7 (P7), reaching a plateau of activity on postnatal day P14. In line with observations made in the hepatocytes, PIDDosome activation in CMs is dependent on PIDD1 localization to extra centrosomes in cells that fail cytokinesis via the distal appendage protein ANKRD26. Interestingly, but in contrast to prior observations in hepatocytes, the PIDDosome limits CM polyploidization in a p53-independent manner but still involves the CDK-inhibitor, *p21/Cdkn1a*, a notion supported by nuclear RNA sequencing and genetic analyses. Together these results provide a new mechanism how proliferation of polyploid CMs is restricted during development, adding new mechanistic insight into the tightly regulated program of terminal differentiation events occurring in the postnatal heart.

Keywords: PIDDosome, Centrosomes, Cardiomyocyte polyploidization, Heart development

1. Introduction

Ischemic heart disease (IHD) is one of the leading causes of mortality worldwide with nearly 9 million deaths documented in 2017[1]. The primary cause of a reduced heart function is the initial loss of cardiomyocytes (CMs) and the inability of humans to compensate it[2,3]. In order to reverse this loss, induction of proliferation in pre-existing CMs appears to be a promising approach but is still not applicable due to a clear gap of knowledge of the terminal differentiation process. This terminal differentiation program is activated postnatally and is characterized by several tightly regulated steps in order to generate mature and functional CMs. After birth, CMs undergo a decrease in cell cycle activity, which is coupled with a change of metabolism from glycolysis to fatty acid oxidation, and an increased maturation status of the sarcomere apparatus[4,5]. In rodents, within the first postnatal week, the majority of CMs fail cytokinesis during mitosis resulting in binucleated CMs[2,6]. At the same time, CMs lose centrosome integrity leading to centriole disengagement, fragmentation of the pericentriolar matrix (PCM), and the translocation of the major microtubule organizing center (MTOC) function from the centrosome to the nuclear envelope[7]. In the second to third postnatal week, a last wave of DNA synthesis occurs in a small subpopulation of binucleated CMs resulting in increased nuclear ploidy in a fraction of cells[8]. Consequently, the adult mouse and rat heart consist of ~80 to 90% binucleated CMs, while the adult human heart contains an estimated ~25% binucleated and ~25 to 40% polyploid mononucleated CMs[2,9–11]

Recent studies showed that the number of polyploid CMs limits cardiac regeneration by reducing the proliferation capacity of CMs[12,13]. However, why polyploid CMs are unable to re-enter the cell cycle is still unknown. Therefore, a better understanding of mechanisms controlling CM polyploidization is of great interest to uncover new avenues for the treatment of heart disease based on the induction of CM proliferation.

A common feature of mononucleated and binucleated polyploid cells is the presence of supernumerary centrosomes[14]. Centrosomes act as the major microtubule organizing center (MTOC) in most animal cells and form the mitotic spindle poles[15]. Thus, tight control of centrosome copy number is critical for faithful chromosome segregation. A diploid cell contains exactly one centrosome that is duplicated once per cell cycle. In contrast, polyploid cells accumulate centrosomes with each round of incomplete cell division. The centrosome is formed by two centrioles, the mother and the daughter centriole, which are surrounded by the pericentriolar matrix. The mother centriole differs from the daughter centriole as it bears distal and subdistal appendages, including the distal appendage proteins ODF2, CEP83, SCLT1 and ANKRD26[16]. The presence of supernumerary centrosomes, as found in polyploid cells, can

alter bipolar spindle organization and metaphase plate formation by acquiring ectopic MTOC activity and thus, creating extra spindle poles[17,18]. This can result in mitotic delays and even chromosome missegregation and thus aneuploidy, which may lead to cell death or senescence[19,20] . To avoid multipolar spindle formation, cells can cluster the extra centrosomes to form a pseudo-bipolar spindle, which can improve but not fully rescue mitotic fidelity[20 21]. Postnatal binucleated CMs show extra centrosomes. In fact, ~ 65% of P3 binucleated CMs contain 4 centrioles, while ~ 27% have 3 centrioles, with 2 mother centrioles[22]. Moreover, once stimulated with pro-proliferative factors in vitro, P3 binucleated CM can re-enter the cell cycle resulting in either a binucleated cell or a mononucleated cell[22]. In both situations, the nuclear ploidy of the resulting daughter CM is believed to increase. This shows that polyploid CMs have the intrinsic capability to cycle but efforts to induce this process in adults have largely failed.

Polyploid cells with extra centrosomes undergo a p53-dependent cell cycle arrest or cell death response [23,24]. This is initially mediated by the "PIDDosome"[25]. The PIDDosome is a multiprotein complex formed by the auto-processed form of PIDD1 (P53-Induced death domain protein 1), termed PIDD1-CC, which recruits the bipartite adapter RAIDD/CRADD (RIP-Associated ICH1/CED3-homologous protein with Death Domain), and the pro-form of Caspase-2, a member of the family of cysteine-driven proteases known to control cell death and inflammation[26]. PIDD1 localizes to the mother centrioles via the distal appendage protein ANKRD26. The presence and clustering of supernumerary mother centrioles result in the activation of this signaling complex, leading to Caspase-2 activation[27,28]. Active Caspase-2 proteolytically inactivates MDM2, the master regulator of cellular p53 levels, and thereby stabilizes p53 protein to promotes a p21-dependent cell cycle arrest[25].

Although first described in cancer cells forced to fail cytokinesis[25], absence of either Caspase-2, RAIDD, or PIDD1, similar to p53 loss itself, increases ploidy in murine primary hepatocytes as part of a physiological polyploidization program during liver organogenesis. Interestingly, the same study has shown that this function of the PIDDosome is preserved also during liver regeneration, and likely also in humans[29]. Altogether, this supports the notion that the PIDDosome is the key player in limiting scheduled as well as accidental polyploidization events via p53 in (non)-cancerous cultured epithelial cells as well as in hepatocytes during liver organogenesis and regeneration[29]. These findings raise the question of whether the PIDDosome is also involved in controlling the scheduled polyploidization of CMs during postnatal heart development, opening new perspectives on heart regeneration therapies based on the induction of CM proliferation by targeting the PIDDosome.

138 **2. Methods**

139 **Animals**

140 The generation and genotyping of *Casp2*$^{-/-}$, *Casp2*$^{fl/fl}$, *Raidd*$^{-/-}$, *Pidd1*$^{-/-}$*mT/mG*, *p53*$^{-/-}$ and *p21*$^{-/-}$
141 mice was previously described[30–36]. *XMLC2-Cre* (*XMLC2*$^{+}$) mice were a kind gift from Prof.
142 Felix Engel[37] . In order to generate *XMLC2*$^{+}$*Casp2*$^{fl/fl}$*mice*, *XMLC2*$^{+}$ mice were crossed with
143 the *Casp2*$^{fl/fl}$ mouse line and bred for more than 10 generations. *XMLC2*$^{+}$mice were crossed
144 with a switchable Tomato and GFP reporter allele (mT/mG) in the Rosa26 locus, allowing
145 expression of membrane bound versions of both fluorescent proteins. The mice used were
146 backcrossed onto C57BL/6N backgrounds for at least 12 generations and handled at the
147 Medical University of Innsbruck Animal Facility. *Ankrd26*$^{-/-}$ mice were generated, maintained
148 and genotyped as previously described[38] and heart tissues were kindly provided by Prof.
149 Andrew J. Holland. In all experiments, age-matched animals were used indiscriminate of sex.

150 **Adult and postnatal cardiomyocyte isolation**

151 Adult hearts from 3-month-old animals of the indicated genotypes were sacrificed by CO2
152 asphyxiation and cervical dislocation according the governmental and international guidelines
153 on animal experimentation. Adult cardiomyocytes were isolated by following the protocol of a
154 Langendorff-free method published by Ackers-Johnson and colleagues[39] with minor changes.
155 To the Collagenase buffer, 30 µM $CaCl_2$ was freshly added to optimize the digestion step. In
156 order to have a final concentration of 0.5 mg/ml, Collagenase II (255 units/mg, 17101-015, Life
157 Technologies, USA) and Collagenase IV (310 units/mg, 17104-019, Life Technologies) were
158 used at 16.52 mg and 16.81 mg, respectively, as the unit concentrations of these enzymes were
159 different from the original protocol. Moreover, the freshly made collagenase buffer, was pre-
160 warmed on a heating magnetic stirrer at 37°C just before being injected in the left ventricle
161 (LV). As first step, 7 ml of EDTA buffer was injected into the apex of the right ventricle with
162 1ml/min speed as described in the original protocol. Then, 20 ml EDTA buffer was injected
163 into the LV over 10 minutes, and subsequently 3 ml of Perfusion buffer was injected into the
164 LV with 1 ml/min speed. 40 ml of Collagenase buffer was finally injected into the LV over 13
165 minutes. However, after 8 minutes the heart was examined to see whether it has lost its color
166 and structure and if it appeared over-digested. If this was the case, the digestion step was
167 stopped at 8 minutes. After heart digestion and creating ~1 mm^3 pieces, the tissue trituration
168 was done by gently pipetting for 4 minutes, followed by the addition of Stop buffer and further
169 gentle pipetting for another 4 minutes. Adult cardiomyocyte vitality was checked after each
170 isolation via Trypan blue staining. In order to assess cellular ploidy, cells were then centrifuged

171 for 2 min at 100 x g, fixed in 4%PFA diluted in PBS for 20 mins at RT and then washed 3 times
172 with PBS.
173 Hearts from postnatal day 1 (P1), P7 and P10 mice from the C57BL/6N mouse strain were
174 dissected upon decapitation with operating scissors (RS-6845, ROBOZ, USA), the atria were
175 removed, and the remaining ventricles were minced. For the isolation of postnatal
176 cardiomyocytes, mouse hearts were isolated and digested utilizing the gentleMACS
177 Dissociation kit (130-098-373, Milteny Biotech GmbH, Germany) according to the
178 manufacturer's instructions. For cardiomyocyte enrichment, cells were pre-plated in DMEM-
179 F12/Glutamax TM-I (10565, Life Technologies)/10% fetal bovine serum (FBS, F0804, Sigma-
180 Aldrich, USA)/penicillin (100 U/ml)/streptomycin (100 µg/ml) (Pen/Strep, P0781, Sigma-
181 Aldrich). After 1.5 h, non-attached cells, enriched in cardiomyocytes, were collected,
182 centrifuged for 10 min at 300 x g, resuspended in DMEM-F12, Glutamax TM-I containing 3
183 mM Na-pyruvate, 0.2% BSA, 0.1 mM ascorbic acid, 0.5% Insulin-Transferrin-Selenium (100x,
184 41400045, Life Technologies), 1% FBS, penicillin/streptomycin (100 U/mg/ml) and counted.
185 Postnatal cardiomyocytes were washed once with PBS (14190169, Thermo Fisher Scientific,
186 USA) and the cell pellet was snap-frozen in liquid nitrogen to preserve RNAs.
187 **Cardiomyocyte nuclei isolation and flow cytometric analyses**
188 The isolation of CM nuclei was performed by following the previously described protocol[40,41]
189 with minor changes. Snap-frozen ventricles from selected genotypes were cut in 1 mm^3 pieces
190 and transferred into a falcon containing 15 ml of lysis buffer and then, homogenized with a TP
191 18/10 Ultra-Turrax probe homogenizer (IKA, Germany) at 20 000 rpm for 20s. In order to
192 isolate the CM nuclei, the 15 ml lysis buffer solution with the homogenized tissues was passed
193 8 times up-and -down through a 20 ml syringe with a 20 G needle. The crude nuclei isolate was
194 filtered using at first, a 100 µm cell strainer, and subsequently, a 70 µm cell strainer. After
195 centrifugation for 10 min at 700 x g at 4°C, the nuclei pellet was dissolved in 5 ml sucrose
196 buffer and then, topped up to 20 ml total solution. 10 ml sucrose buffer was added into a 1%
197 BSA/PBS pre-coated ultra-centrifuge tube and was overlayed by the 20 ml nuclei suspension
198 before spinning for 60 min at 13 000 x g at 4°C. After centrifugation over sucrose, buffer was
199 quickly removed and the nuclei were resuspended in 700 µl of nuclei storage buffer. Next, 600
200 µl of nuclei solution was incubated with a rabbit anti-PCM1 antibody (1:300, HPA023370, lot.
201 number: 000007967, Sigma-Aldrich,) overnight at 4°C with constant shaking. 100 µl of the
202 nuclei solution was used for the negative control of the staining. On the next day, both nuclei
203 samples were washed by adding 2 ml of PBS, centrifuged for 10 min at 700 x g at 4°C and then,
204 the nuclei pellets were incubated with goat anti-rabbit Alexa 647-conjugated antibodies (1:500,

205 Life Technologies) for 60 min at 4°C. After 1 hour, the samples were washed with PBS and
206 incubated with Propidium Iodide (1:25 of a 1 mg/ml solution). The gating strategy for ploidy
207 analysis is shown in Suppl. Figure 1A, nuclear DNA content was measured on a flow cytometer
208 (LSR-Fortessa, BD Biosystems, USA) and data were analyzed quantitatively, excluding
209 doublets, using FlowJo (FlowJo X, LLC).

210 **Immunohistology**

211 In order to have cardiomyocytes in a relax status (diastole), hearts were injected with a
212 cardioplegic solution (25 mmol/L KCl) in the LV. Once the hearts stopped beating, they were
213 cut from the aorta branch and placed in 4% PFA diluted in PBS overnight at RT. On the next
214 day the fixed hearts were dehydrated and paraffinized. For hematoxylin and eosin staining, 4
215 µm frontal heart sections were deparaffinized and rehydrated by repeated xylol and ethanol
216 incubation steps and stained. At least 6 different hearts per genotype were analyzed. After the
217 staining, sections were mounted and images acquired on NanoZoomer S210 Digital slide
218 scanner (C13239-01, Hamamatsu photonics, Japan).

219 **Cryosections**

220 Hearts from mentioned genotypes were pre-fixed in 4% PFA overnight at 4°C and on the next
221 day, washed 3 times with PBS and incubated in 15% sucrose diluted in MilliQ water for 4 hat
222 4°. After the 15% Sucrose solution, hearts were submerged in 30% sucrose diluted in MilliQ
223 water overnight at 4°C. Afterwards, hearts were embedded in Tissue-Tek O.C.T. compound
224 tissue-freezing medium (4583, Sekura, Germany), frozen in liquid nitrogen, and sectioned with
225 a Microm HM550 (Thermo Fischer Scientific) (10 µm). Once the tissues were cut, the sections
226 were left to better adhere on the slide for 30 min at RT.

227 **Immunofluorescence analyses**

228 Immunostainings were performed as previously described[42], with an additional centrifugation
229 step for 2 min at 100 x g at RT. Before antibody incubation, freshly isolated and PFA-fixed
230 CMs were permeabilized with 0.5% Triton X-100/PBS for 10 min at RT. Primary antibodies:
231 rabbit anti-Pan cadherin (1:100, C3678, Sigma-Aldrich,), mouse anti-sarcomeric-µ-actinin
232 (1:200, ab9465, Abcam). After overnight incubation, primary antibodies were detected by using
233 Alexa Fluor™ 488 , Alexa Fluor™ 594 or Alexa Fluor™ 647 conjugated antibodies (1:500,
234 Life Technologies, USA). DNA was visualized with SYTOX™ Green Nucleic Acid Stain
235 (1:200,000 in PBS with 0.1% triton and 10% horse serum, S7020, Thermo Fisher Scientific).
236 Samples were diluted in PBS in order to acquire pictures. Confocal images were captured on a
237 spinning disk confocal laser scanning microscope (Cell Voyager CV1000, Yokogawa, Tokyo,
238 Japan).

239 FFPE heart sections were boiled in antigen retrieval buffer (1 mM EDTA, pH 8.0) for 8 min
240 in a microwave (700W). After the antigen retrieval step, slides were kept for 30 min at RT and
241 rinsed 3 times in PBS. Next, the slides were incubated in WGA (1:100 diluted in PBS, W11261,
242 Thermo Fisher Scientific,) for 10 min at RT and then, washed 2 times with PBS. After this step,
243 immunostainings were performed as previously described (29522098). As primary antibody a
244 goat anti-Troponin I (1:500, ab56357, Abcam) was used, which was detected by an Alexa
245 Fluor™ 594 conjugated antibody (1:500, Life Technologies, USA). DNA was visualized with
246 0.5 µg/ml DAPI (4′,6′-diamidino-2-phenylindole) (Sigma Aldrich). Samples were mounted
247 with Fluoromount-G™ (Thermo Fisher Scientific). Images were captured on a Zeiss Axiovert
248 200 M microscope using the VisiView 4.1.0.3 (Visitron Systems) acquisition software.
249 Immunostainings of pre-fixed heart cryosections were permeabilized with 0.5% Triton in PBS
250 for 10 min at RT. Subsequently, the above-mentioned immunostaining protocol[42] was used with
251 a minor modification of the time of secondary antibody incubation, set to 1h at RT. High
252 resolution images were captured on a LSM980 confocal laser scanning microscope (ZEISS,
253 Germany).

254 **RNA isolation and qRT-PCR**

255 Postnatal CM pellets were processed in order to extract total RNA using TRIzol TM Reagent
256 (15596018, Invitrogen, USA) according to the manufacturer. 1µg of total RNA was used for
257 generation of cDNA (iScript cDNA synthesis kit, 170–8891, BioRad, USA). For quantitative
258 real-time PCR (RT-qPCR) experiments 140 ng of cDNA per each reaction was used. RT-qPCR
259 assays were performed in experimental triplicates for each biological replicate using Luna®
260 Universal Probe One-Step RT-qPCR Kit (E3006, New England biolabs, USA) in a StepOne
261 Plus real time PCR system (Applied Biosystems, USA). Relative gene expression was
262 calculated based on ΔCt values using *mGapdh* as housekeeping gene.

263 **Bulk nuclear RNA sequencing (RNAseq) analysis**

264 For extraction of nuclear CM RNA, postnatal cardiomyocyte nuclei were isolated and stained
265 using anti-PCM1, as described above. Subsequently, cardiomyocyte nuclei were sorted based
266 on their PCM1 staining by using a BD FACSAria™ III Cell Sorter (648282, BD Bioscience).
267 Importantly, in order to obtain enough RNA material from the isolated cardiomyocyte nuclei,
268 several hearts from the same postnatal days were pooled together per biological replicate (P1:
269 15 hearts, P7: 6 hearts, P14: 2 hearts). Afterwards, the low-binding Eppendorf tubes containing
270 the sorted cardiomyocyte nuclei were centrifuged for 10 min at 700 x g at 4°C. The resulting
271 nuclei pellets were processed for RNA extraction by utilizing the Quick-RNA MicroPrep Kit
272 (R1050, Zymo Research, USA) following the manufacturer's protocol. RNA-sequencing

library were prepared by Lexogen NGS Services (Vienna, Austria) using the QuantSeq 3′ mRNA-Seq Library Prep Kit FWD for Illumina and following the low-input protocol. Sequencing was preformed on an Illumina NextSeq 2000 at Lexogen NGS Services to produce 100bp single-end reads for each sample. Raw RNA sequencing reads were quality-controlled with FastQC (v0.11.8)[43] and preprocessed with cutadapt (v4.0)[44] to trim poly-G stretches resembling sequencing artefacts, trim low-quality bases from the 3'end, trim adapter and poly-A sequences introduced by the sequencing strategy, remove low-quality reads (more than 1 expected error and/or more than 30% N-bases) and remove short reads (less than 20 nucleotides). Processed reads were aligned against the mouse reference genome GRCm39 from Ensembl (v108)[45] using STAR (v2.6.1e)[46]. All following analyses were performed within R v. 4.2.1. The number of reads per gene (considering the full gene, i.e. both exonic and intronic sequences) was counted with HTSeq (v2.0.3)[47]. Gene count normalization and differential gene expression analysis were performed with the R package limma (v. 3.52.4)[48]. Genes were considered as significantly differentially expressed with an adjusted p-value < 0.05 and an absolute log2 fold change > 1. Gene set enrichment analysis was carried out using the R package gage (v. 2.46.1)[49], based on a selection of gene sets retrieved with the R package msigdbr (v. 7.5.1)[50] (included gene set collections: hallmark, canonical pathways excluding WikiPathways, transcription factor targets, Gene Ontology). Gene sets were considered as differentially expressed when presenting with a plain p-value < 0.05.

Bulk ncRNA sequencing data pre-processing and analysis

Before gene count normalization, differential gene expression analysis, and all subsequent analysis steps were performed as described above. Three samples (P1 *XMLC2^{-}Casp2$^{fl/fl}$* replicate 1, P14 *XMLC2^{-}Casp2$^{fl/fl}$* replicate 3, P14 *XMLC^{+}Casp2$^{fl/fl}$* replicate 1) were excluded due to low quality. The number of detected genes (at least one read count) was particularly low for P14 *XMLC2^{-}Casp2$^{fl/fl}$* replicate 3 (1676 genes) and P14 *XMLC^{+}Casp2$^{fl/fl}$* replicate 1 (3893 genes) compared to the other samples (between 7223 and 17057 genes) (data not shown). P1 *XMLC2^{-}Casp2$^{fl/fl}$* replicate 1 clustered particularly far away in a PCA of all samples (PCA calculated with R package labdsv v2.1-0[51] (Suppl. Figure 3A). A fuzzy clustering of all samples showed clusters of genes (clusters 6 and 7) with high expression level in P1 *XMLC2^{-}Casp2$^{fl/fl}$* replicate 1 compared to replicates 2, 3, and 4 (fuzzy clustering performed with R package Mfuzz v2.56.0[52] (Suppl. Figure 4). The clustering was calculated on the gene log2 fold changes with respect to the average gene counts of the four P1 *XMLC2^{-}Casp2$^{fl/fl}$* replicates, after each sample's raw counts were normalized with the average count of its interquartile range count values. Subsequent functional enrichment analysis of gene cluster 6 and cluster 7 returned

307 significantly enriched gene sets (adjusted p-value < 0.05) associated with mitochondria,
308 ribosomes and translation (Suppl. Figure 3B). Functional enrichment was calculated with
309 Fisher's exact test, based on the same gene set collection as described above. As these results
310 are indicative of a cytoplasmic contamination of P1 *XMLC2*$^{-}$*Casp2*$^{fl/fl}$ replicate 1, this sample
311 was not considered for further analysis.

312 **Imaris image analysis**

313 Nuclear and cellular ploidy measurements were performed by following the indications
314 published by Bensley and colleagues[11]. More in detail, firstly, reconstituting the individual
315 nuclei by the 3D volume module ("3D View" in Imaris) was accomplished and then, analyzing
316 the mean intensity of the Sytox Green was achieved by using the "surface" Imaris software
317 package. Importantly, since signal intensity is fundamental for accurate ploidy measurement,
318 the same setting of laser power, voltage, offset, and pinhole across the board was kept constant
319 for all the experiments. Single nuclei from binucleated CMs were taken as reference for diploid
320 nuclei in this analysis. For nuclear and cellular ploidy analysis, images were captured on a
321 spinning disk confocal microscope, CV1000 Cell voyager (Yokogawa, Japan).

322 **Statistical analysis**

323 Data are expressed as the mean ± standard deviation (SD) or standard error of the mean (SEM)
324 of at least three independent experiments if not stated otherwise. Statistical significance of
325 differences was evaluated by either Student's t test, or 1way or 2way ANOVA followed by
326 Bonferroni's post-hoc test, Sidak's or Tukey's multiple comparisons test (GraphPad Prism 9.0).
327 $p < 0.05$ was considered as statistically significant.
328
329

330 **3. Results**

331 **The PIDDosome controls cardiomyocyte ploidy**

332 In order to decipher the role of the PIDDosome during CM polyploidization, we quantified the
333 nuclear ploidy of freshly-isolated CMs from 3-month-old mice lacking individual PIDDosome
334 components (Figure 1A). The ploidy of single CM nuclei was assessed by 3D volumetric
335 analysis of Sytox Green fluorescence intensity and correlated with the cellular ploidy status.
336 Moreover, the nuclear staining intensity of single nuclei from binucleated CMs, representing
337 the majority of cells isolated from WT hearts, was used to define 2N ploidy[11]. This analysis
338 revealed that CM nuclei of binucleated cells from all three different PIDDosome knockout
339 strains contain a higher percentage of nuclei with increased DNA staining intensity, compared
340 to nuclei from binucleated CMs from WT hearts. This suggests that binucleated CMs in *Pidd1,*
341 *Raidd* and *Casp2 deficient* animals harbor an increased number of nuclei with > 2N DNA
342 content (Figure 1B). To determine the exact nuclear ploidy of single CM nuclei from
343 PIDDosome-mutant animals, we used a flow cytometry-based strategy. To discriminate CM
344 nuclei from non-myocyte nuclei, we exploited the translocation of the pericentriolar matrix
345 protein PCM1 from the centrosome to the nuclear envelope during terminal CM differentiation[7]
346 (Suppl. Figure 1A). Intriguingly, PIDDosome-mutant animals showed a more than two-fold
347 increase in the percentage of tetraploid (4n) CM nuclei, compared to those isolated from WT
348 animals (Figure 1C). Quantification of the cellular ploidy status of CMs showed that absence
349 of the PIDDosome also causes a significant increase in multinucleated CMs (Figure 1D).
350 Together, these results indicate that abrogation of the PIDDosome induces a pronounced
351 increase in nuclear as well as cellular polyploidization of CM. This suggests that in the absence
352 of the PIDDosome, tetraploid binucleated CMs enter another round of cell cycle, characterized
353 by cytokinesis failure generating either octoploid binucleated CMs or multinucleated CMs with
354 diploid single CM nuclei.

355 To test if this phenotype is independent of external parameters, e.g., non-myocytes influencing
356 postnatal CM polyploidization, we generated a mouse mutant harboring a cardiac specific
357 deletion of *Casp2* exploiting a floxed *Caspase-2* allele and a *XLMC2-Cre* transgene
358 ($XMLC2^{+}Casp2^{fl/fl}$) (Suppl. Figure 1B). To test if cardiac CRE expression alters CM
359 polyploidization and to ensure its cardiac-specificity, *XMLC2-Cre* mice were first crossed with
360 a fluorescence reporter line, carrying a switchable Tomato and GFP reporter allele (*mT/mG*) in
361 the Rosa26 locus allowing expression of membrane bound versions of both fluorescent proteins.
362 In the *mT/mG* model, all cells initially express the Tomato reporter prior to CRE recombination,
363 but not GFP. CRE protein expression leads to excision of both the Tomato cassette and the

364 STOP signal, allowing expression of membrane-bound GFP (Suppl. Figure 1C). Consistently,
365 upon *XMLC2*-driven CRE activation, CM membranes in heart cryo-sections were GFP-
366 positive, while non-CM membranes retained dTomato positivity. Staining with α-sarcomeric
367 actinin and DAPI was performed in addition to define cell identity and nuclear morphology
368 (Figure 1E). CRE expression under control of the *XMLC2* promoter did not affect CM nuclear
369 ploidy (Suppl. Figure 1D). Similar to full body *Casp2*$^{-/-}$ mice, 3D volumetric analysis of Sytox
370 Green staining intensity, as well as flow cytometric analysis using DAPI revealed that cardiac-
371 specific Caspase-2 deletion *in XMLC2*$^{+}$*Casp2*$^{fl/fl}$ mice significantly increased the percentage
372 of polyploid CM nuclei, when compared to *Casp2*$^{fl/fl}$ control mice lacking CRE expression
373 (*XMLC2*$^{-}$*Casp2*$^{fl/fl}$) (Figure 1F,G). In addition, the cellular ploidy of *XMLC2*$^{+}$*Casp2*$^{fl/fl}$ CMs
374 increased to a similar degree as for the full body *Casp2*$^{-/-}$ animals (Figure 1H).
375 Taken together, these data indicate that the PIDDosome controls CM polyploidization,
376 limiting not only their nuclear but also cellular ploidy in a cell autonomous manner.
377
378 **Increased CM ploidy does not affect cardiac structure or function**
379 Since PIDDosome loss causes an increase of polyploid CMs in adulthood, we wondered
380 whether this might affect the heart structure and thus, cardiac function. The heart ultra-structure
381 of the different genotypes was analyzed by hematoxylin and eosin (H&E) staining on frontal
382 sections of formalin-fixed and paraffin-embedded (FFPE) hearts. No obvious differences were
383 observed in *Casp2*$^{-/-}$, *Raidd*$^{-/-}$ or *Pidd1*$^{-/-}$ hearts compared to WT hearts (Figure 2A), as well as
384 in *XMLC2*$^{+}$ *Casp2*$^{fl/fl}$ *vs*. *XMLC2*$^{-}$ *Casp2*$^{fl/fl}$ (Suppl. Figure 1E). Likewise, echocardiography of
385 7-10-week old mice lacking *Pidd1* confirmed that the observed increases in the polyploid CM
386 population did not affect the cardiac function. In fact, there were no significant differences in
387 ejection fraction (EF) and fractional shortening (FS) between *Pidd1*$^{-/-}$ and WT mice (Figure 2B-
388 C).
389 Polyploid cells harbor multiple copies of the DNA content, and they are usually larger than
390 their diploid counterparts[53]. Since ablation of PIDDosome components causes an increase in
391 polyploid CM, we wanted to investigate whether this ploidy increase was associated with an
392 increase of CM area. For this reason, frontal sections of (FFPE) hearts from *Casp2*$^{-/-}$, *Raidd*$^{-/-}$,
393 *Pidd1*$^{-/-}$ and WT mice were stained for a membrane marker, Wheat germ agglutinin (WGA), a
394 cardiac marker, Troponin I and DAPI. Quantification of the cross-sectional area of CMs
395 revealed no differences across genotypes, (Figure 2 D), suggesting that increases of ploidy are
396 not associated with an increase in CM size, even though contrasting findings were made in the
397 liver[54].

398 Collectively, these data show that PIDDosome deletion and the subsequent increases in
399 the number of polyploid CM do not alter the tissue architecture of the heart and more
400 importantly, cardiac function in steady state.
401
402 **The PIDDosome restricts cardiomyocyte ploidy in early postnatal development**
403 Cardiomyocytes fail to undergo cytokinesis, thus becoming binucleated during the first week
404 after birth[3,10]. As described by Alkass and colleagues[8], a second wave of polyploidization
405 occurs between the second and the third postnatal week. To define when the PIDDosome may
406 be engaged during cardiomyocyte development, we first evaluated postnatal mRNA expression
407 of the individual PIDDosome components by qRT-PCR. All PIDDosome components showed
408 low expression levels at P1, while at P7 mRNA levels of all components were found strongly
409 increased. Interestingly, decreasing expression of these genes already at P10 suggest that the
410 PIDDosome components are under tight transcriptional control during heart development
411 (Figure 3A). Next, we examined the exact time-point of PIDDosome-mediated CM-specific
412 ploidy control, hearts from WT, *Casp2*$^{-/-}$, *Raidd*$^{-/-}$ and *Pidd1*$^{-/-}$ mice were isolated on P1, P7,
413 P14 and P21, and CM nuclear ploidy was assessed by flow cytometry. As expected, on P1 no
414 significant difference in the fraction of tetraploid CM nuclei was observed across genotypes
415 (Figure 3B), consistent with diploid mononucleated CMs dominating at this developmental
416 stage[3]. However, at P7 the population of tetraploid CM nuclei in PIDDosome mutant mice
417 increased compared to the same population in WT mice (Figure 3C). This coincides with the
418 formation of binucleated CM at this time point during heart development, as previously
419 reported[3]. Interestingly, the percentage of tetraploid CM nuclei reached a plateau at P14 as no
420 further increases were noted on P21 (Figure 3D-E), matching numbers were seen in adult mice
421 (Fig. 1C). Flow cytometric ploidy analysis of *XMLC2*$^{+}$*Casp2*$^{fl/fl}$ mice confirmed that this is a
422 cell-autnonomous effect (Figure 3F).
423 Collectively, these data show that the PIDDosome controls CM polyploidization as
424 early as P7.
425
426 **Ploidy control in CM depends on extra centrosomes**
427 PIDDosome activation depends on PIDD1 binding to extra mother centrioles via the centriolar
428 distal appendage protein ANKRD26 in cancer cells[55], as well as in primary hepatocytes[38].
429 Notably, previous work has shown that ~ 65% of binucleated CMs on postnatal day 3 (P3)
430 contain 4 centrioles with extra mother centrioles, while ~ 27% have 3 centrioles[22]. To evaluate
431 the relationship of PIDDosome activation and centrosomes, we quantified the CM nuclear

ploidy in 3-month-old *Ankrd26* knockout hearts. Indeed, the percentage of tetraploid nuclei in *Ankrd26*$^{-/-}$ mice was increased by two-fold, similar to what was observed in the PIDDosome knockout mice (Figure 4A). This strongly suggests that the PIDDosome regulates CM polyploidization based on centrosome number via PIDD1 localization to the centriolar distal appendage protein ANKRD26.

Caspase-2-deficient CMs show enhanced expression signatures related to proliferation

In order to elucidate the biological processes through which the PIDDosome executes its ploidy-regulating function in CMs, CM nuclei of P1, P7 and P14 from *XMLC2*$^{-}$*Casp2*$^{fl/fl}$ (control mice) and *XMLC2*$^{+}$*Casp2*$^{fl/fl}$ mice were sorted based on PCM1 staining to perform bulk RNAseq (Suppl. Figure 2A). Gene set enrichment analysis results of control CMs supported the previously described developmental changes between P1, P7 and P14[56,57] . In fact, different ion channels were upregulated in P14 compared to P7 in gene-set enrichment analysis, which is a known feature of cardiomyocyte maturation[58,59]. In addition, gene sets associated with cell adhesion were upregulated in P1 compared to P7 CMs, as previously published[57]. Gene sets of RNA splicing, aerobic respiration and oxidative phosphorylation were abundant in P7 CMs in both comparisons, P14 *vs.* P7 and P7 *vs.* P1, as a sign of cardiomyocyte maturation[60]. Interestingly, when comparing nuclear transcriptomes of CMs isolated from P7 *vs.* P1, gene sets such as mitochondrial protein-containing complexes, as well as mitochondrion organization_ were upregulated, indicating that P7 CMs have a more mature mitochondria structure or organization compared to P1 CMs, as previously shown[59,61] (Suppl. Figure 2B-C). In addition, a tendency towards the expression of genes, which play a role in sarcomere structure and regulation, previously associated with cardiomyocyte developmental maturation[57,59], was also noted between P1 and P7 CMs (Suppl. Figure 2D). Since the PIDDosome starts to control CM ploidy status during the first week postnatally (Figure 3), we investigated the differentially expressed genes of Casp2-depleted CMs (*XMLC2*$^{+}$*Casp2*$^{fl/fl}$ mice) compared to CMs from control animals (*XMLC2*$^{-}$*Casp2*$^{fl/fl}$ mice) at P7 (Figure 4B). Interestingly, genes related to CM proliferation (*Foxm1*[62–64], *Gas5*[65,66], *Sqle*[67], *Dusp8*[68], cell cycle regulation (*Cdkn1a*[69], *Hes1*[70], *Trim39*[71], *Lin37*[72], *Kif18a*[73,74]), ploidy control (*E2F8*[75], *MAD2L1*[76]) and T-Tubule maturation (*Bin1*[77]) were found statistically and significantly altered between genotypes (Figure 4C). Further, gene set enrichment analysis highlighted that GO terms related to chromosome separation, mitotic spindle checkpoint, PLK1 pathway, resolution of sister-chromatid cohesion and microtubule-based processes, were upregulated in *Casp2*-depleted CMs *vs.* CMs from control mice on P7, suggesting that Caspase-2-depleted CMs, which are more polyploid compared to their P7 control counterparts (Figure 1), might experience mitotic errors and delays

466 due to their increased DNA content. Importantly, downregulated GO terms in P7 Casp2-
467 depleted CMs *vs.* P7 control CMs were associated with a reduction in fatty acid metabolism
468 and muscle differentiation as well as sarcomere organization (Figure 4C), proposing that CMs
469 lacking Caspase-2 might delay the naturally occurring terminal differentiation program,
470 containing more immature and cycling CMs compared to control mice at that developmental
471 stage.

472 **CM ploidy control does not require p53 pathway activity**

473 Mechanistically, the PIDDosome regulates ploidy by the activation of the protease activity of
474 Caspase-2 and subsequent MDM2 cleavage and its key-components are negatively regulated
475 by E2F8, consistent with hits in our bulk nuclear (nc)RNAseq analysis. As this axis is conserved
476 across several cell types[25,29], we investigated whether it is also at play in CM polyploidization.
477 To this end, we analyzed CM ploidy in 3-month-old *p53*$^{-/-}$ mice. Surprisingly, the percentage
478 of tetraploid CM nuclei in mice lacking this key ploidy regulator was not significantly different
479 compared to WT animals. In the liver, p53 promotes a p21 induced cell cycle arrest in polyploid
480 hepatocytes[29]. Intriguingly, *p21*$^{-/-}$ mice showed a significant increase in ploidy, compared over
481 WT animals. Curiously, the percentage of 4N nuclei in *p21*$^{-/-}$ mice was still lower compared to
482 that seen the PIDDosome knockout mice (~16 % *vs.* ~28%, respectively), suggesting that
483 PIDDosome controls CM ploidy through another route than the canonical MDM2-p53-p21 axis
484 or that p21 and the PIDDosome may act in separate pathways (Figure 4D). However, comparing
485 CM nuclei from *Caspase-2* mutant mice with those from *Caspase-2/p21* double-knockout
486 animals did not reveal an additional ploidy increase, suggesting that p21 acts downstream of
487 the PIDDosome.

488 Taken together, these data indicate that the PIDDosome exerts its CM ploidy controlling
489 function depending on extra centrosomes but independently of p53 stabilization, yet engaging
490 p21 in a yet to be defined manner. The transcriptomic profiles of Casp2-depleted CMs suggest
491 that the PIDDosome influences not only the CM cell cycle directly by modulating CM-specific
492 and general cell cycle/ploidy genes, but also indirectly by altering other biological processes,
493 such as lipid metabolism and CM differentiation, which are known to regulate CM
494 proliferation[57,59,78]. As such, we propose that the PIDDosome represents an attractive target to
495 modulate CM differentiation and possibly regeneration.

496

497

498

499

502 **4. Discussion**

503 During early postnatal development, cardiomyocytes lose their proliferative capacity and
504 become polyploid, which is an established barrier to heart regeneration. To date, little is known
505 about why polyploid cardiomyocytes cannot re-enter the cell cycle. Here, we show that the
506 PIDDosome multiprotein complex is critical for regulating cardiomyocyte polyploidization. In
507 fact, mice lacking individual PIDDosome components exhibit an increased nuclear and cellular
508 ploidy status of cardiomyocytes, which does not alter cardiac functionality and structure in
509 steady-state. This PIDDosome-mediated cardiomyocyte-specific ploidy control is restricted to
510 the first weeks after birth. Importantly, our data suggest that this pathway is activated in
511 polyploid CMs by "counting" supernumerary centrioles via the localization of PIDD1 with
512 ANKRD26. Interestingly, in CMs the PIDDosome limits polyploidy independently of p53
513 stabilization, but still involves p21. As Casp2/p21 double-mutant animals show no additional
514 ploidy increase, we conclude that p21 is epistatic downstream of Caspase-2. How Caspase-2
515 can engage p21 in the absence of p53 is unclear. P73 has been implicated in regulating CM
516 proliferation and is also regulated by MDM2 and may compensate for p53 during postnatal
517 heart development[79,80], Moreover, stabilizing effects of Caspase-2 on p21 mRNA translation
518 have also been reported[81]). Regardless of mechanism, these data together with the increased
519 level of 4N cardiomyocyte nuclei in *p21* knockout animals suggest that the PIDDosome might
520 exert its function not exclusively via p21, as the increase in 4N cardiomyocyte nuclei in *p21*
521 knockout mice is consistently slightly lower than in PIDDosome-deficient CMs. These findings
522 are in line with previous studies which have shown that postnatal cardiomyocyte proliferation
523 depends on p21[82] but not on p53, as a *p53* knockout is insufficient to induce cardiomyocyte
524 proliferation[83].

525 E2F8 is known to be a fundamental regulator of hepatocyte ploidy during liver development[75]
526 where it transcriptionally targets *Casp2* and *Pidd1*[29]. Recently, it was reported that
527 cardiomyocyte-specific double knockout of E2F8 and E2F7 mice have an increased percentage
528 of mononucleated diploid cardiomyocytes, which had no effect on cardiac function in steady
529 state but also failed to improve heart regeneration after infarction[84]. Our bulk RNAseq data has
530 shown that cardiac-specific deletion of Caspase-2 correlates with an upregulation of *E2f8,*
531 which could explain the increased level of polyploid cardiomyocyte in these mice, as E2F8
532 mediated suppression of cytokinesis genes may be more effective. In addition, it seems that the
533 limited change of cardiomyocyte ploidy observed both in *E2f7/8* and PIDDosome knockout
534 mice, does not cause alteration in cardiac function suggests a rather broad range of CM ploidy
535 is compatible with the maintenance of heart function and regeneration. The reported association

536 of lower CM ploidy and increased regenerative capacity across a large range of genetic
537 backgrounds in mice[13] needs to be explored further.
538 Finally, heart regeneration therapies based on cardiomyocyte proliferation face many obstacles
539 in clinical studies and hence it seems worth-while to explore if induction of polyploid
540 cardiomyocyte proliferation is a possible strategy, and if this can be achieved by PIDDosome
541 inhibition. Of notice, small molecules targeting Caspase-2 have been reported[85–87] and thus,
542 their validation in preclinical studies is of great interest.
543
544
545
546

Funding

ML acknowledges support by the Austrian Science Fund (FWF) (Lisa Meitner, M 3115-B), AV acknowledges support by the FWF (P36658), as well as the ERC, AdG 787171 (POLICE). FE acknowledges support from the DOC fellowship program of the Austrian Academy of Sciences (ÖAW).

Acknowledgements

We would like to thank Claudia Soratroi, Irene Gaggl and Julia Heppke for technical support, and Martin Saurwein and Maria Fischer for animal care, Vincent Braun for help with cryo-sections, as well as Bergmann Olaf, TU-Dresden, DE, for critical discussion and AndrewJ Holland (Baltimore) and Felix Engel (Erlangen) for heart tissue from *Ankrd26-/-* and *XMLC2-Cre* mice, respectively.

Conflict of Interest

None declared.

562 **References**

563 1. Virani, S.S., Alonso, A., Benjamin, E.J., Bittencourt, M.S., Callaway, C.W., Carson, A.P.,
564 Chamberlain, A.M., Chang, A.R., Cheng, S., Delling, F.N., et al. (2020). Heart Disease and Stroke
565 Statistics-2020 Update: A Report From the American Heart Association. Circulation *141*, E139–
566 E596. https://doi.org/10.1161/CIR.0000000000000757.

567 2. Leone, M., Magadum, A., and Engel, F.B. (2015). Cardiomyocyte proliferation in cardiac
568 development and regeneration: a guide to methodologies and interpretations. Am. J. Physiol.
569 Heart Circ. Physiol. *309*, H1237–H1250. https://doi.org/10.1152/AJPHEART.00559.2015.

570 3. Leone, M., and Engel, F.B. (2019). Advances in heart regeneration based on cardiomyocyte
571 proliferation and regenerative potential of binucleated cardiomyocytes and polyploidization.
572 Clin. Sci. (Lond). *133*, 1229–1253. https://doi.org/10.1042/CS20180560.

573 4. Guo, Y., and Pu, W.T. (2020). Cardiomyocyte Maturation: New Phase in Development at
574 Lippincott Williams and Wilkins, https://doi.org/10.1161/CIRCRESAHA.119.315862
575 https://doi.org/10.1161/CIRCRESAHA.119.315862.

576 5. Maroli, G., and Braun, T. (2021). The long and winding road of cardiomyocyte maturation.
577 Cardiovasc. Res. *117*, 712–726. https://doi.org/10.1093/CVR/CVAA159.

578 6. Derks, W., and Bergmann, O. (2020). Polyploidy in Cardiomyocytes: Roadblock to Heart
579 Regeneration? Circ. Res. *126*, 552–565. https://doi.org/10.1161/CIRCRESAHA.119.315408.

580 7. Zebrowski, D.C., Vergarajauregui, S., Wu, C.C., Piatkowski, T., Becker, R., Leone, M., Hirth, S.,
581 Ricciardi, F., Falk, N., Giessl, A., et al. (2015). Developmental alterations in centrosome
582 integrity contribute to the post-mitotic state of mammalian cardiomyocytes. Elife *4*.
583 https://doi.org/10.7554/ELIFE.05563.

584 8. Alkass, K., Panula, J., Westman, M., Wu, T. Di, Guerquin-Kern, J.L., and Bergmann, O. (2015).
585 No Evidence for Cardiomyocyte Number Expansion in Preadolescent Mice. Cell *163*, 1026–
586 1036. https://doi.org/10.1016/J.CELL.2015.10.035.

587 9. Mollova, M., Bersell, K., Walsh, S., Savla, J., Das, L.T., Park, S.Y., Silberstein, L.E., Dos Remedios,
588 C.G., Graham, D., Colan, S., et al. (2013). Cardiomyocyte proliferation contributes to heart
589 growth in young humans. Proc. Natl. Acad. Sci. U. S. A. *110*, 1446–1451.
590 https://doi.org/10.1073/pnas.1214608110.

591 10. Soonpaa, M.H., Kim, K.K., Pajak, L., Franklin, M., and Field, L.J. (1996). Cardiomyocyte DNA
592 synthesis and binucleation during murine development. Am. J. Physiol. *271*.
593 https://doi.org/10.1152/AJPHEART.1996.271.5.H2183.

594 11. Bensley, J.G., De Matteo, R., Harding, R., and Black, M.J. (2016). Three-dimensional direct
595 measurement of cardiomyocyte volume, nuclearity, and ploidy in thick histological sections.
596 Sci. Rep. *6*. https://doi.org/10.1038/SREP23756.

597 12. González-Rosa, J.M., Sharpe, M., Field, D., Soonpaa, M.H., Field, L.J., Burns, C.E., and Burns,
598 C.G. (2018). Myocardial Polyploidization Creates a Barrier to Heart Regeneration in Zebrafish.
599 Dev. Cell *44*, 433-446.e7. https://doi.org/10.1016/J.DEVCEL.2018.01.021.

600 13. Patterson, M., Barske, L., Van Handel, B., Rau, C.D., Gan, P., Sharma, A., Parikh, S., Denholtz,
601 M., Huang, Y., Yamaguchi, Y., et al. (2017). Frequency of mononuclear diploid cardiomyocytes
602 underlies natural variation in heart regeneration. Nat. Genet. *49*, 1346–1353.
603 https://doi.org/10.1038/NG.3929.

604 14. Jusino, S., Fernández-Padín, F.M., and Saavedra, H.I. (2018). Centrosome aberrations and
605 chromosome instability contribute to tumorigenesis and intra-tumor heterogeneity. J. cancer
606 metastasis Treat. *4*, 43. https://doi.org/10.20517/2394-4722.2018.24.

607 15. Bettencourt-Dias, M. (2013). Q&A: Who needs a centrosome? BMC Biol. *11*.
608 https://doi.org/10.1186/1741-7007-11-28.

609 16. Bowler, M., Kong, D., Sun, S., Nanjundappa, R., Evans, L., Farmer, V., Holland, A., Mahjoub,
610 M.R., Sui, H., and Loncarek, J. (2019). High-resolution characterization of centriole distal
611 appendage morphology and dynamics by correlative STORM and electron microscopy. Nat.
612 Commun. *10*. https://doi.org/10.1038/S41467-018-08216-4.

613 17. Marthiens, V., Piel, M., and Basto, R. (2012). Never tear us apart--the importance of
614 centrosome clustering. J. Cell Sci. *125*, 3281–3292. https://doi.org/10.1242/JCS.094797.

615 18. Watanabe, K., Takao, D., Ito, K.K., Takahashi, M., and Kitagawa, D. (2019). The Cep57-
616 pericentrin module organizes PCM expansion and centriole engagement. Nat. Commun. *10*.
617 https://doi.org/10.1038/S41467-019-08862-2.

618 19. Navarro-Serer, B., Childers, E.P., Hermance, N.M., Mercadante, D., and Manning, A.L. (2019).
619 Aurora A inhibition limits centrosome clustering and promotes mitotic catastrophe in cells
620 with supernumerary centrosomes. Oncotarget *10*, 1649–1659.
621 https://doi.org/10.18632/ONCOTARGET.26714.

622 20. Nigg, E.A., Čajánek, L., and Arquint, C. (2014). The centrosome duplication cycle in health and
623 disease. FEBS Lett. *588*, 2366–2372. https://doi.org/10.1016/J.FEBSLET.2014.06.030.

624 21. Milunović-Jevtić, A., Mooney, P., Sulerud, T., Bisht, J., and Gatlin, J.C. (2016). Centrosomal
625 clustering contributes to chromosomal instability and cancer. Curr. Opin. Biotechnol. *40*, 113–

626 118. https://doi.org/10.1016/J.COPBIO.2016.03.011.

627 22. Leone, M., and Engel, F.B. (2019). Pseudo-bipolar spindle formation and cell division in
628 postnatal binucleated cardiomyocytes. J. Mol. Cell. Cardiol. *134*, 69–73.
629 https://doi.org/10.1016/J.YJMCC.2019.07.005.

630 23. Davoli, T., and De Lange, T. (2011). The causes and consequences of polyploidy in normal
631 development and cancer. Annu. Rev. Cell Dev. Biol. *27*, 585–610.
632 https://doi.org/10.1146/ANNUREV-CELLBIO-092910-154234.

633 24. Pfau, S.J., and Amon, A. (2012). Chromosomal instability and aneuploidy in cancer: from yeast
634 to man. EMBO Rep. *13*, 515–527. https://doi.org/10.1038/EMBOR.2012.65.

635 25. Fava, L.L., Schuler, F., Sladky, V., Haschka, M.D., Soratroi, C., Eiterer, L., Demetz, E., Weiss, G.,
636 Geley, S., Nigg, E.A., et al. (2017). The PIDDosome activates p53 in response to supernumerary
637 centrosomes. Genes Dev. *31*, 34–45. https://doi.org/10.1101/GAD.289728.116/-/DC1.

638 26. Fava, L.L., Bock, F.J., Geley, S., and Villunger, A. (2012). Caspase-2 at a glance. J. Cell Sci. *125*,
639 5911–5915. https://doi.org/10.1242/JCS.115105.

640 27. Evans, L.T., Anglen, T., Scott, P., Lukasik, K., Loncarek, J., and Holland, A.J. (2021). ANKRD26
641 recruits PIDD1 to centriolar distal appendages to activate the PIDDosome following
642 centrosome amplification. EMBO J. *40*. https://doi.org/10.15252/EMBJ.2020105106.

643 28. Burigotto, M., Mattivi, A., Migliorati, D., Magnani, G., Valentini, C., Roccuzzo, M., Offterdinger,
644 M., Pizzato, M., Schmidt, A., Villunger, A., et al. (2021). Centriolar distal appendages activate
645 the centrosome-PIDDosome-p53 signalling axis via ANKRD26. EMBO J. *40*.
646 https://doi.org/10.15252/EMBJ.2020104844.

647 29. Sladky, V.C., Knapp, K., Soratroi, C., Heppke, J., Eichin, F., Rocamora-Reverte, L., Szabo, T.G.,
648 Bongiovanni, L., Westendorp, B., Moreno, E., et al. (2020). E2F-Family Members Engage the
649 PIDDosome to Limit Hepatocyte Ploidy in Liver Development and Regeneration. Dev. Cell *52*,
650 335-349.e7. https://doi.org/10.1016/J.DEVCEL.2019.12.016.

651 30. Berube, C., Boucher, L.M., Ma, W., Wakeham, A., Salmena, L., Hakem, R., Yeh, W.C., Mak,
652 T.W., and Benchimol, S. (2005). Apoptosis caused by p53-induced protein with death domain
653 (PIDD) depends on the death adapter protein RAIDD. Proc. Natl. Acad. Sci. U. S. A. *102*,
654 14314–14319. https://doi.org/10.1073/PNAS.0506475102.

655 31. Kim, J.Y., Wang, L.Q., Sladky, V.C., Oh, T.G., Liu, J., Trinh, K., Eichin, F., Downes, M., Hosseini,
656 M., Jacotot, E.D., et al. (2022). PIDDosome-SCAP crosstalk controls high-fructose-diet-
657 dependent transition from simple steatosis to steatohepatitis. Cell Metab. *34*, 1548-1560.e6.

658 https://doi.org/10.1016/J.CMET.2022.08.005.

659 32. Brugarolas, J., Chandrasekaran, C., Gordon, J.I., Beach, D., Jacks, T., and Hannon, G.J. (1995).
660 Radiation-induced cell cycle arrest compromised by p21 deficiency. Nature *377*, 552–557.
661 https://doi.org/10.1038/377552A0.

662 33. Lowe, S.W., Schmitt, E.M., Smith, S.W., Osborne, B.A., and Jacks, T. (1993). p53 is required for
663 radiation-induced apoptosis in mouse thymocytes. Nature *362*, 847–849.
664 https://doi.org/10.1038/362847A0.

665 34. Manzl, C., Krumschnabel, G., Bock, F., Sohm, B., Labi, V., Baumgartner, F., Logette, E.,
666 Tschopp, J., and Villunger, A. (2009). Caspase-2 activation in the absence of PIDDosome
667 formation. J. Cell Biol. *185*, 291–303. https://doi.org/10.1083/JCB.200811105.

668 35. O'Reilly, L.A., Ekert, P., Harvey, N., Marsden, V., Cullen, L., Vaux, D.L., Hacker, G., Magnusson,
669 C., Pakusch, M., Cecconi, F., et al. (2002). Caspase-2 is not required for thymocyte or neuronal
670 apoptosis even though cleavage of Caspase-2 is dependent on both Apaf-1 and caspase-9. Cell
671 Death Differ. *9*, 832–841. https://doi.org/10.1038/SJ.CDD.4401033.

672 36. Muzumdar, M.D., Tasic, B., Miyamichi, K., Li, N., and Luo, L. (2007). A global double-
673 fluorescent Cre reporter mouse. Genesis *45*, 593–605. https://doi.org/10.1002/DVG.20335.

674 37. Breckenridge, R., Kotecha, S., Towers, N., Bennett, M., and Mohun, T. (2007). Pan-myocardial
675 expression of Cre recombinase throughout mouse development. Genesis *45*, 135–144.
676 https://doi.org/10.1002/DVG.20275.

677 38. Sladky, V.C., Akbari, H., Tapias-Gomez, D., Evans, L.T., Drown, C.G., Strong, M.A., LoMastro,
678 G.M., Larman, T., and Holland, A.J. (2022). Centriole signaling restricts hepatocyte ploidy to
679 maintain liver integrity. Genes Dev. *36*, 843–856. https://doi.org/10.1101/GAD.349727.122/-
680 /DC1.

681 39. Ackers-Johnson, M., Li, P.Y., Holmes, A.P., O'Brien, S.M., Pavlovic, D., and Foo, R.S. (2016). A
682 Simplified, Langendorff-Free Method for Concomitant Isolation of Viable Cardiac Myocytes
683 and Nonmyocytes From the Adult Mouse Heart. Circ. Res. *119*, 909–920.
684 https://doi.org/10.1161/CIRCRESAHA.116.309202.

685 40. Bergmann, O., and Jovinge, S. (2012). Isolation of cardiomyocyte nuclei from post-mortem
686 tissue. J. Vis. Exp. https://doi.org/10.3791/4205.

687 41. Bergmann, O., Zdunek, S., Felker, A., Salehpour, M., Alkass, K., Bernard, S., Sjostrom, S.L.,
688 Szewczykowska, M., Jackowska, T., Dos Remedios, C., et al. (2015). Dynamics of Cell
689 Generation and Turnover in the Human Heart. Cell *161*, 1566–1575.

690 https://doi.org/10.1016/J.CELL.2015.05.026.

691 42. Leone, M., Musa, G., and Engel, F.B. (2018). Cardiomyocyte binucleation is associated with
692 aberrant mitotic microtubule distribution, mislocalization of RhoA and IQGAP3, as well as
693 defective actomyosin ring anchorage and cleavage furrow ingression. Cardiovasc. Res. *114*,
694 1115–1131. https://doi.org/10.1093/CVR/CVY056.

695 43. Andrews, S. (2010). FastQC: A Quality Control tool for High Throughput Sequence Data.

696 44. Martin, M. (2011). Cutadapt removes adapter sequences from high-throughput sequencing
697 reads. EMBnet.journal *17*, 10–12. https://doi.org/10.14806/EJ.17.1.200.

698 45. Harrison, P.W., Amode, M.R., Austine-Orimoloye, O., Azov, A.G., Barba, M., Barnes, I., Becker,
699 A., Bennett, R., Berry, A., Bhai, J., et al. (2024). Ensembl 2024. Nucleic Acids Res. *52*, D891–
700 D899. https://doi.org/10.1093/NAR/GKAD1049.

701 46. Dobin, A., Davis, C.A., Schlesinger, F., Drenkow, J., Zaleski, C., Jha, S., Batut, P., Chaisson, M.,
702 and Gingeras, T.R. (2013). STAR: Ultrafast universal RNA-seq aligner. Bioinformatics *29*, 15–21.
703 https://doi.org/10.1093/bioinformatics/bts635.

704 47. Putri, G.H., Anders, S., Pyl, P.T., Pimanda, J.E., and Zanini, F. (2022). Analysing high-throughput
705 sequencing data in Python with HTSeq 2.0. Bioinformatics *38*, 2943–2945.
706 https://doi.org/10.1093/BIOINFORMATICS/BTAC166.

707 48. Ritchie, M.E., Phipson, B., Wu, D., Hu, Y., Law, C.W., Shi, W., and Smyth, G.K. (2015). limma
708 powers differential expression analyses for RNA-sequencing and microarray studies. Nucleic
709 Acids Res. *43*, e47–e47. https://doi.org/10.1093/NAR/GKV007.

710 49. Luo, W., Friedman, M.S., Shedden, K., Hankenson, K.D., and Woolf, P.J. (2009). GAGE:
711 generally applicable gene set enrichment for pathway analysis. BMC Bioinformatics *10*.
712 https://doi.org/10.1186/1471-2105-10-161.

713 50. Dolgalev, I. (2022). msigdbr: MSigDB Gene Sets for Multiple Organisms in a Tidy Data Format.
714 https://igordot.github.io/msigdbr/.

715 51. Roberts, D.W. (2023). Ordination and Multivariate Analysis for Ecology.

716 52. Kumar, L., and Futschik, M.E. (2007). Mfuzz: A software package for soft clustering of
717 microarray data. Bioinformation *2*, 5. https://doi.org/10.6026/97320630002005.

718 53. Unhavaithaya, Y., and Orr-Weaver, T.L. (2012). Polyploidization of glia in neural development
719 links tissue growth to blood-brain barrier integrity. Genes Dev. *26*, 31–36.
720 https://doi.org/10.1101/GAD.177436.111.

721 54. Wang, M.J., Chen, F., Lau, J.T.Y., and Hu, Y.P. (2017). Hepatocyte polyploidization and its
722 association with pathophysiological processes. Cell Death Dis. *8*.
723 https://doi.org/10.1038/CDDIS.2017.167.

724 55. Burigotto, M., Mattivi, A., Migliorati, D., Magnani, G., Valentini, C., Roccuzzo, M., Offterdinger,
725 M., Pizzato, M., Schmidt, A., Villunger, A., et al. (2021). Centriolar distal appendages activate
726 the centrosome-PIDDosome-p53 signalling axis via ANKRD26. EMBO J. *40*, 1–22.
727 https://doi.org/10.15252/embj.2020104844.

728 56. Baniol, M., Murganti, F., Smialowska, A., Panula, J., Lázár, E., Brockman, V., Giatrellis, S.,
729 Derks, W., and Bergmann, O. (2021). Identification and characterization of distinct cell cycle
730 stages in cardiomyocytes using the FUCCI transgenic system. Exp. Cell Res. *408*.
731 https://doi.org/10.1016/J.YEXCR.2021.112880.

732 57. Quaife-Ryan, G.A., Sim, C.B., Ziemann, M., Kaspi, A., Rafehi, H., Ramialison, M., El-Osta, A.,
733 Hudson, J.E., and Porrello, E.R. (2017). Multicellular Transcriptional Analysis of Mammalian
734 Heart Regeneration. Circulation *136*, 1123–1139.
735 https://doi.org/10.1161/CIRCULATIONAHA.117.028252.

736 58. Harrell, M.D., Harbi, S., Hoffman, J.F., Zavadil, J., and Coetzee, W.A. (2007). Large-scale
737 analysis of ion channel gene expression in the mouse heart during perinatal development.
738 Physiol. Genomics *28*, 273–283. https://doi.org/10.1152/PHYSIOLGENOMICS.00163.2006.

739 59. Talman, V., Teppo, J., Pöhö, P., Movahedi, P., Vaikkinen, A., Tuuli Karhu, S., Trošt, K.,
740 Suvitaival, T., Heikkonen, J., Pahikkala, T., et al. (2018). Molecular Atlas of Postnatal Mouse
741 Heart Development. J. Am. Heart Assoc. *7*. https://doi.org/10.1161/JAHA.118.010378.

742 60. Lopaschuk, G.D., and Jaswal, J.S. (2010). Energy metabolic phenotype of the cardiomyocyte
743 during development, differentiation, and postnatal maturation. J. Cardiovasc. Pharmacol. *56*,
744 130–140. https://doi.org/10.1097/FJC.0B013E3181E74A14.

745 61. Garbern, J.C., and Lee, R.T. (2021). Mitochondria and metabolic transitions in cardiomyocytes:
746 lessons from development for stem cell-derived cardiomyocytes. Stem Cell Res. Ther. *12*.
747 https://doi.org/10.1186/S13287-021-02252-6.

748 62. Zuppo, D.A., Missinato, M.A., Santana-Santos, L., Li, G., Benos, P. V., and Tsang, M. (2023).
749 Foxm1 regulates cardiomyocyte proliferation in adult zebrafish after cardiac injury.
750 Development *150*. https://doi.org/10.1242/DEV.201163.

751 63. Zhang, Z., Freeman, M., Zhang, Y., El-Nachef, D., Davenport, G., Williams, A., and MacLellan,
752 W.R. (2023). Hippo signaling and histone methylation control cardiomyocyte cell cycle re-

753 entry through distinct transcriptional pathways. PLoS One *18*.
754 https://doi.org/10.1371/JOURNAL.PONE.0281610.

755 64. Cheng, Y., Yan, Y., Lundy, D.J., Lo, A.H., Wang, Y., Ruan, S., Lin, P., and Hsieh, P.C. (2017).
756 Reprogramming-derived gene cocktail increases cardiomyocyte proliferation for heart
757 regeneration. EMBO Mol. Med. *9*, 251–264. https://doi.org/10.15252/EMMM.201606558.

758 65. Zhou, X.H., Chai, H.X., Bai, M., and Zhang, Z. (2020). LncRNA-GAS5 regulates PDCD4 expression
759 and mediates myocardial infarction-induced cardiomyocytes apoptosis via targeting MiR-21.
760 Cell Cycle *19*, 1363–1377. https://doi.org/10.1080/15384101.2020.1750257.

761 66. See, K., Tan, W.L.W., Lim, E.H., Tiang, Z., Lee, L.T., Li, P.Y.Q., Luu, T.D.A., Ackers-Johnson, M.,
762 and Foo, R.S. (2017). Single cardiomyocyte nuclear transcriptomes reveal a lincRNA-regulated
763 de-differentiation and cell cycle stress-response in vivo. Nat. Commun. *8*.
764 https://doi.org/10.1038/S41467-017-00319-8.

765 67. Mills, R.J., Parker, B.L., Quaife-Ryan, G.A., Voges, H.K., Needham, E.J., Bornot, A., Ding, M.,
766 Andersson, H., Polla, M., Elliott, D.A., et al. (2019). Drug Screening in Human PSC-Cardiac
767 Organoids Identifies Pro-proliferative Compounds Acting via the Mevalonate Pathway. Cell
768 Stem Cell *24*, 895-907.e6. https://doi.org/10.1016/J.STEM.2019.03.009.

769 68. Maillet, M., Purcell, N.H., Sargent, M.A., York, A.J., Bueno, O.F., and Molkentin, J.D. (2008).
770 DUSP6 (MKP3) null mice show enhanced ERK1/2 phosphorylation at baseline and increased
771 myocyte proliferation in the heart affecting disease susceptibility. J. Biol. Chem. *283*, 31246–
772 31255. https://doi.org/10.1074/JBC.M806085200.

773 69. El-Deiry, W.S. (2016). p21(WAF1) Mediates Cell-Cycle Inhibition, Relevant to Cancer
774 Suppression and Therapy. Cancer Res. *76*, 5189–5191. https://doi.org/10.1158/0008-
775 5472.CAN-16-2055.

776 70. Maeda, Y., Isomura, A., Masaki, T., and Kageyama, R. (2023). Differential cell-cycle control by
777 oscillatory versus sustained Hes1 expression via p21. Cell Rep. *42*.
778 https://doi.org/10.1016/J.CELREP.2023.112520.

779 71. Zhang, L., Mei, Y., Fu, N.Y., Guan, L., Xie, W., Liu, H.H., Yu, C.D., Yin, Z., Yu, V.C., and You, H.
780 (2012). TRIM39 regulates cell cycle progression and DNA damage responses via stabilizing
781 p21. Proc. Natl. Acad. Sci. U. S. A. *109*, 20937–20942.
782 https://doi.org/10.1073/PNAS.1214156110.

783 72. Mages, C.F.S., Wintsche, A., Bernhart, S.H., and Müller, G.A. (2017). The DREAM complex
784 through its subunit Lin37 cooperates with Rb to initiate quiescence. Elife *6*.

785 https://doi.org/10.7554/ELIFE.26876.

786 73. Fonseca, C.L., Malaby, H.L.H., Sepaniac, L.A., Martin, W., Byers, C., Czechanski, A., Messinger,
787 D., Tang, M., Ohi, R., Reinholdt, L.G., et al. (2019). Mitotic chromosome alignment ensures
788 mitotic fidelity by promoting interchromosomal compaction during anaphase. J. Cell Biol. *218*,
789 1148–1163. https://doi.org/10.1083/JCB.201807228.

790 74. Marquis, C., Fonseca, C.L., Queen, K.A., Wood, L., Vandal, S.E., Malaby, H.L.H., Clayton, J.E.,
791 and Stumpff, J. (2021). Chromosomally unstable tumor cells specifically require KIF18A for
792 proliferation. Nat. Commun. *12*. https://doi.org/10.1038/S41467-021-21447-2.

793 75. Pandit, S.K., Westendorp, B., Nantasanti, S., Van Liere, E., Tooten, P.C.J., Cornelissen, P.W.A.,
794 Toussaint, M.J.M., Lamers, W.H., and De Bruin, A. (2012). E2F8 is essential for polyploidization
795 in mammalian cells. Nat. Cell Biol. *14*, 1181–1191. https://doi.org/10.1038/NCB2585.

796 76. Sotillo, R., Hernando, E., Díaz-Rodríguez, E., Teruya-Feldstein, J., Cordón-Cardo, C., Lowe, S.W.,
797 and Benezra, R. (2007). Mad2 overexpression promotes aneuploidy and tumorigenesis in
798 mice. Cancer Cell *11*, 9–23. https://doi.org/10.1016/J.CCR.2006.10.019.

799 77. Perdreau-Dahl, H., Lipsett, D.B., Frisk, M., Kermani, F., Carlson, C.R., Brech, A., Shen, X.,
800 Bergan-Dahl, A., Hou, Y., Tuomainen, T., et al. (2023). BIN1, Myotubularin, and Dynamin-2
801 Coordinate T-Tubule Growth in Cardiomyocytes. Circ. Res. *132*, E188–E205.
802 https://doi.org/10.1161/CIRCRESAHA.122.321732.

803 78. Li, Z., Yao, F., Yu, P., Li, D., Zhang, M., Mao, L., Shen, X., Ren, Z., Wang, L., and Zhou, B. (2022).
804 Postnatal state transition of cardiomyocyte as a primary step in heart maturation. Protein Cell
805 *13*, 842–862. https://doi.org/10.1007/S13238-022-00908-4.

806 79. Klein, A.M., Biderman, L., Tong, D., Alaghebandan, B., Plumber, S.A., Mueller, H.S., Van
807 Vlimmeren, A., Katz, C., and Prives, C. (2021). MDM2, MDMX, and p73 regulate cell-cycle
808 progression in the absence of wild-type p53. Proc. Natl. Acad. Sci. U. S. A. *118*, e2102420118.
809 https://doi.org/10.1073/PNAS.2102420118/SUPPL_FILE/PNAS.2102420118.SAPP.PDF.

810 80. Ebelt, H., Zhang, Y., Köhler, K., Xu, J., Gajawada, P., Boettger, T., Hollemann, T., Müller-
811 Werdan, U., Werdan, K., and Braun, T. (2008). Directed expression of dominant-negative p73
812 enables proliferation of cardiomyocytes in mice. J. Mol. Cell. Cardiol. *45*, 411–419.
813 https://doi.org/10.1016/J.YJMCC.2008.06.006.

814 81. Sohn, D., Budach, W., and Jänicke, R.U. (2011). Caspase-2 is required for DNA damage-
815 induced expression of the CDK inhibitor p21WAF1/CIP1. Cell Death Differ. 2011 1810 *18*,
816 1664–1674. https://doi.org/10.1038/cdd.2011.34.

817 82. Engel, F.B., Hauck, L., Boehm, M., Nabel, E.G., Dietz, R., and von Harsdorf, R. (2003). p21(CIP1)
818 Controls proliferating cell nuclear antigen level in adult cardiomyocytes. Mol. Cell. Biol. *23*,
819 555–565. https://doi.org/10.1128/MCB.23.2.555-565.2003.

820 83. Stanley-Hasnain, S., Hauck, L., Grothe, D., Aschar-Sobbi, R., Beca, S., Butany, J., Backx, P.H.,
821 Mak, T.W., and Billia, F. (2017). p53 and Mdm2 act synergistically to maintain cardiac
822 homeostasis and mediate cardiomyocyte cell cycle arrest through a network of microRNAs.
823 Cell Cycle *16*, 1585–1600. https://doi.org/10.1080/15384101.2017.1346758.

824 84. Yu, Z., Zhang, L., Cattaneo, P., Guimarães-Camboa, N., Fang, X., Gu, Y., Peterson, K.L.,
825 Bogomolovas, J., Cuitino, C., Leone, G.W., et al. (2023). Increasing Mononuclear Diploid
826 Cardiomyocytes by Loss of E2F Transcription Factor 7/8 Fails to Improve Cardiac Regeneration
827 After Infarct. Circulation *147*, 183–186.
828 https://doi.org/10.1161/CIRCULATIONAHA.122.061018.

829 85. Bosc, E., Anastasie, J., Soualmia, F., Coric, P., Kim, J.Y., Wang, L.Q., Lacin, G., Zhao, K., Patel, R.,
830 Duplus, E., et al. (2022). Genuine selective Caspase-2 inhibition with new irreversible small
831 peptidomimetics. Cell Death Dis. *13*. https://doi.org/10.1038/S41419-022-05396-2.

832 86. Poreba, M., Rut, W., Groborz, K., Snipas, S.J., Salvesen, G.S., and Drag, M. (2019). Potent and
833 selective Caspase-2 inhibitor prevents MDM-2 cleavage in reversine-treated colon cancer
834 cells. Cell Death Differ. 2019 2612 *26*, 2695–2709. https://doi.org/10.1038/s41418-019-0329-
835 2.

836 87. Castellón, J.O., Ofori, S., Burton, N.R., Julio, A.R., Turmon, A.C., Armenta, E., Sandoval, C.,
837 Boatner, L.M., Takayoshi, E.E., Faragalla, M., et al. (2024). Chemoproteomics Identifies State-
838 Dependent and Proteoform-Selective Caspase-2 Inhibitors. J. Am. Chem. Soc. *146*, 14972–
839 14988. https://doi.org/10.1021/JACS.3C12240/SUPPL_FILE/JA3C12240_SI_006.XLSX.

840

841

842 **Figure legends**

843 **Figure 1. The PIDDosome regulates nuclear and cellular polyploidization of**
844 **cardiomyocytes**

845 **(A-B**) Ploidy measurements of single CM nuclei by 3D volumetric analysis of Sytox-green
846 fluorescence intensity in correlation with the cellular ploidy status. **(A)** Representative pictures
847 of freshly-isolated 3-month-old CMs from different genotypes. CMs were stained for the
848 cardiac marker, α-sarcomeric actinin (purple), and a nuclear marker, Sytox-green. Scale bars:
849 10 µm. **(B)** Scatter blots of the fluorescence intensity quantification as in A. n: 4 hearts per
850 genotype; 100 CMs per heart. Data are mean ± SEM; One-way ANOVA with Dunnett's
851 multiple comparisons test. (**C**) Representative histograms (left) and quantification (right) of the
852 CM nuclear ploidy measured by flow cytometry in 3-month-old hearts from the indicated
853 genotypes. n: 7 (WT), n:4 (*Pidd1*$^{-/-}$), n:4 (*Raidd*$^{-/-}$), n:5 (*Casp2*$^{-/-}$). Data (mean ± SD) were
854 analyzed by Two-way ANOVA with Bonferroni post-hoc test. (**D**) Bar graphs showing the CM
855 cellular ploidy at the age of 3 months of the indicated genotypes. n: 4 hearts per genotype. 150
856 CMs per heart were quantified. Data are mean ± SEM; Two-way ANOVA followed by
857 Dunnett's multiple comparisons test. Statistical analysis between the multinucleated group from
858 the different genotypes is shown in the graph. (**E**) Validation of the cardio-specificity of the
859 *XMLC2* promoter. Confocal pictures of cryosections of pre-fixed hearts stained for α-
860 sarcomeric-actinin (purple) and DAPI (grey). Scale bars: 40 µm. (**F**) Quantification of CM
861 nuclear ploidy by 3D volumetric analysis of Sytox-green fluorescence intensity. n: 3 hearts per
862 genotype. 100 CM nuclei per heart were analyzed. Data are mean ± SEM and analyzed by Two-
863 tailed Student's t test. (**G**) Quantification of CM nuclear ploidy by flow-cytometry of 3-month-
864 old mice of the indicated genotypes. n: 4 (*XMLC2*$^{-}$ Casp2$^{fl/fl}$), n: 8 (*XMLC2*$^{+}$ Casp2$^{fl/fl}$). Data
865 are mean ± SD; Two-way ANOVA with Bonferroni post-hoc test. (**H**) Bar graphs showing the
866 CM cellular ploidy of the indicated genotypes at the age of 3 months. n: 3 hearts per genotype;
867 150 CM nuclei per hearts were analyzed. Data are mean ± SEM analyzed by two-way ANOVA
868 followed by Sidak's multiple comparisons test. * $p < 0.05$, ** $p < 0.01$, *** $p < 0.001$ ****: $p <$
869 0.0001, n.s.: not significant.

870

871 **Figure 2. Loss of PIDDosome-dependent CM ploidy regulation does not impact heart**
872 **structure and functionality.**

873 **(A)** Representative images of hematoxylin and eosin (H&E) stained FFPE heart sections of 3-
874 month-old mice of the indicated genotypes. Scale bars: 1mm. (**B-C**) Quantification of the
875 cardiac functions ejection fraction (B) and fractional shortening (C) measured by

876 echocardiography in 3-month-old mice. n: 21 (WT), n: 18 (*Pidd1*$^{-/-}$). Statistical significance was
877 assessed with Student's t test. (**D**) Representative pictures (left) and cross-sectional area
878 quantifications (right) of FFPE hearts from WT, *Pidd1*$^{-/-}$, *Raidd*$^{-/-}$ or *Casp2*$^{-/-}$ mice stained for
879 the membrane marker WGA (green), the cardiac marker Troponin I (red) and DAPI (blue) to
880 visualize nuclei. Scale Bars: 50µm. n: 5 (WT, *Pidd1*$^{-/-}$, *Raidd*$^{-/-}$, *Casp2*$^{-/-}$, ~ 2100 CMs per heart
881 were quantified). Data are mean ± SD, two-way ANOVA with Bonferroni post-hoc test. n.s.:
882 not significant.
883

884 **Figure 3. The PIDDosome controls CM ploidy levels starting on day P7 during heart**
885 **development.**

886 (**A**) Bar graph showing PIDDosome mRNA levels were determined by qRT-PCR in CMs from
887 WT mice isolated at P1, P7 and P10. Data are mean ± SEM analyzed by two-way ANOVA
888 with Bonferroni post-hoc test. n: 3 litters with pooled isolations per postnatal timepoint with 3-
889 5 pooled hearts analyzed. (**B-E**) Quantification of the CM nuclear ploidy measured by flow
890 cytometry of P1 (B), P7 (C), P14 (D) and P21(E) CM nuclei from the indicated genotypes. n:
891 3-5 for P1 (5 hearts of each genotype per n), n: 5 for P7 (3 hearts of each genotype per n), n: 3
892 for P14 (2 hearts of each genotype per n), n: 4-6 for P21 (2 hearts of each genotype per n). Data
893 are mean ± SD analyzed by two-way ANOVA with Bonferroni post-hoc test. (**F**) Quantification
894 of the CM nuclear ploidy as in (B-E) in *XMLC2*$^{-}$*Casp2*$^{fl/fl}$ and *XMLC2*$^{+}$*Casp2*$^{fl/fl}$ mice at P7. n:
895 4 (*XMLC2*$^{-}$*Casp2*$^{fl/fl}$), n: 5 (*XMLC2*$^{+}$*Casp2*$^{fl/fl}$) (n: 3 hearts of each genotype per n). Data are
896 mean ± SD analyzed by two-way ANOVA with Bonferroni post-hoc test. Data are mean ± SD.
897 **p < 0.01, ***p < 0.001, ****p < 0.0001, n.s.: not significant.

898 **Figure 4. PIDDosome-mediated CM ploidy control is downstream of extra centrosomes**
899 **but independent of p53 stabilization**

900 (**A**) Quantification of CM nuclear ploidy of 3-month-old *Ankrd26*$^{-/-}$ and WT (C57BL/6J) mice
901 measured by flow cytometry. n: 4 per genotype. Data are mean ± SD analyzed by two-way
902 ANOVA with Bonferroni post-hoc test. (**B**) Bar graph showing the CM nuclear ploidy of the
903 indicated genotypes as in (A). n: 10 (WT), n:7 (*p21*$^{-/-}$), n:5 (*p53*$^{-/-}$). Data are mean ± SD analyzed
904 by two-way ANOVA with Bonferroni multiple comparison test. ****p < 0.0001, n.s.: not
905 significant. (**C**) Volcano plot showing the differential gene expression analysis comparing
906 *XMLC2*$^{+}$*Casp2*$^{fl/fl}$ to *XMLC2*$^{-}$*Casp2*$^{fl/fl}$ samples at P7. Dashed lines indicate an adj. p-value of
907 0.05 and a log2FC of -1 and 1. Numbers of up- or downregulated differentially expressed genes
908 are indicated in the graph. (**D**) Selected significantly deregulated gene sets of the gene set

909 enrichment analysis results comparing *XMLC*$^{+}$ *Casp2*$^{fl/fl}$ to. *XMLC2*$^{-}$*Casp2*$^{fl/fl}$ samples at P7.
910 Dashed lines represent a plain p-value of 0.05.

911

912 **Supplemental Figure 1. CRE expression under control of the *XMLC2* promoter does not**
913 **affect CM nuclear ploidy.**

914 (**A**) Representative dot plots of the flow cytometry gating strategy used to assess CM nuclear
915 ploidy. Nuclei were isolated from frozen 12 weeks old hearts and CM nuclei were identified as
916 PCM1^{+}. The DNA content of CM nuclei was measured by PI staining. (**B-C**) Schematic
917 illustrations showing the generation of cardiomyocyte-specific deletion of *Casp2* (B) and
918 cardiomyocyte-specific membrane labelling (mT/mG; C) driven by *XMLC2*-dependent Cre
919 activation. (**D**) Bar graph showing the quantification of CM nuclear ploidy measured by flow
920 cytometry of the indicated genotypes. n: 3 (*XMLC2*$^{-}$), 4 (*XMLC2*$^{+}$). Data are mean ± SD
921 analyzed by two-way ANOVA with Sidak post-hoc test; n.s.: not significant. (**E**) Representative
922 H&E stained FFPE heart sections of 3 months old mice of the indicated genotypes. Scale bars:
923 1mm.

924

925 **Supplemental Figure 2. Gene set enrichment analysis results of control CMs supports**
926 **the previously described developmental changes between P1, P7 and P14 CMs.**

927 (**A**) RLDF (regularized linear discriminant functions) representation of the CM RNAseq
928 samples, based on the centered, log2-transformed counts-per-million (log2CPM) (note: before
929 count normalization with limma). The sample groups as indicated in the legend were defined
930 as RLDF training groups. RDLF was performed with the function 'plotRLDF' of the R package
931 limma (v. 3.52.4). (**B-C**) Graphs show selected significantly deregulated gene sets of the gene
932 set enrichment analysis results comparing developmental days in control mice (*XMLC2*$^{-}$
933 *Casp2*$^{fl/fl}$). Dashed lines represent a plain p-value of 0.05. (**D**) Heatmap of selected genes
934 involved in sarcomere structure and regulation. The Z-scores of normalized gene expression
935 calculated across P1 and P7 control samples are shown.

936 **Supplemental Figure 3. Bulk RNA sequencing sample exclusion**

937 (**A**) Principal component analysis (PCA) of the CM RNAseq samples, based on the centered,
938 log2-transformed counts-per-million (log2CPM) (note: before count normalization with
939 limma). The samples are labelled with their respective group and replicate number; for
940 improved readability of the labels, '*XMLC2*$^{-}$ *Casp2*$^{fl/fl}$' was replaced with 'minus' and '*XMLC*$^{+}$

941 *Casp2*$^{fl/fl}$' was replaced with 'plus'. (**B**) Top 20 enriched gene sets (by adjusted p-value) of
942 fuzzy clusters 6 and 7 genes determined by functional enrichment analysis.

943 **Supplemental Figure 4. Fuzzy clustering of all samples**

944 Fuzzy clustering of all CM RNAseq samples. Clustering was performed on the gene log2 fold
945 changes with respect to the average gene counts of the four P1 *XMLC2*$^{-}$ *Casp2*$^{fl/fl}$ replicates,
946 after each sample's raw counts were normalized with the average count of its interquartile
947 range count values.

948

Leone M *et al.* Figure 1

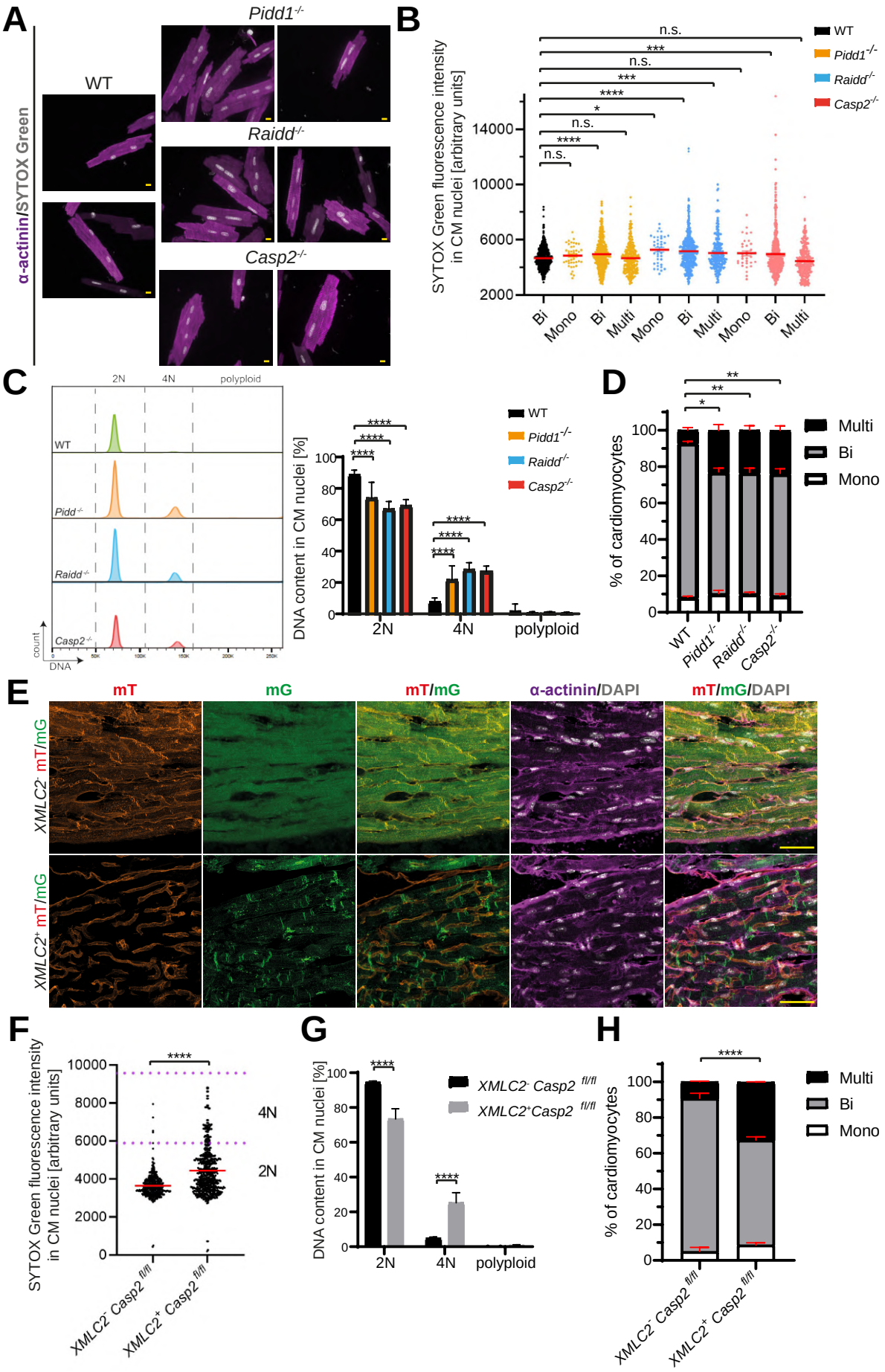

Leone M *et al.* Figure 2

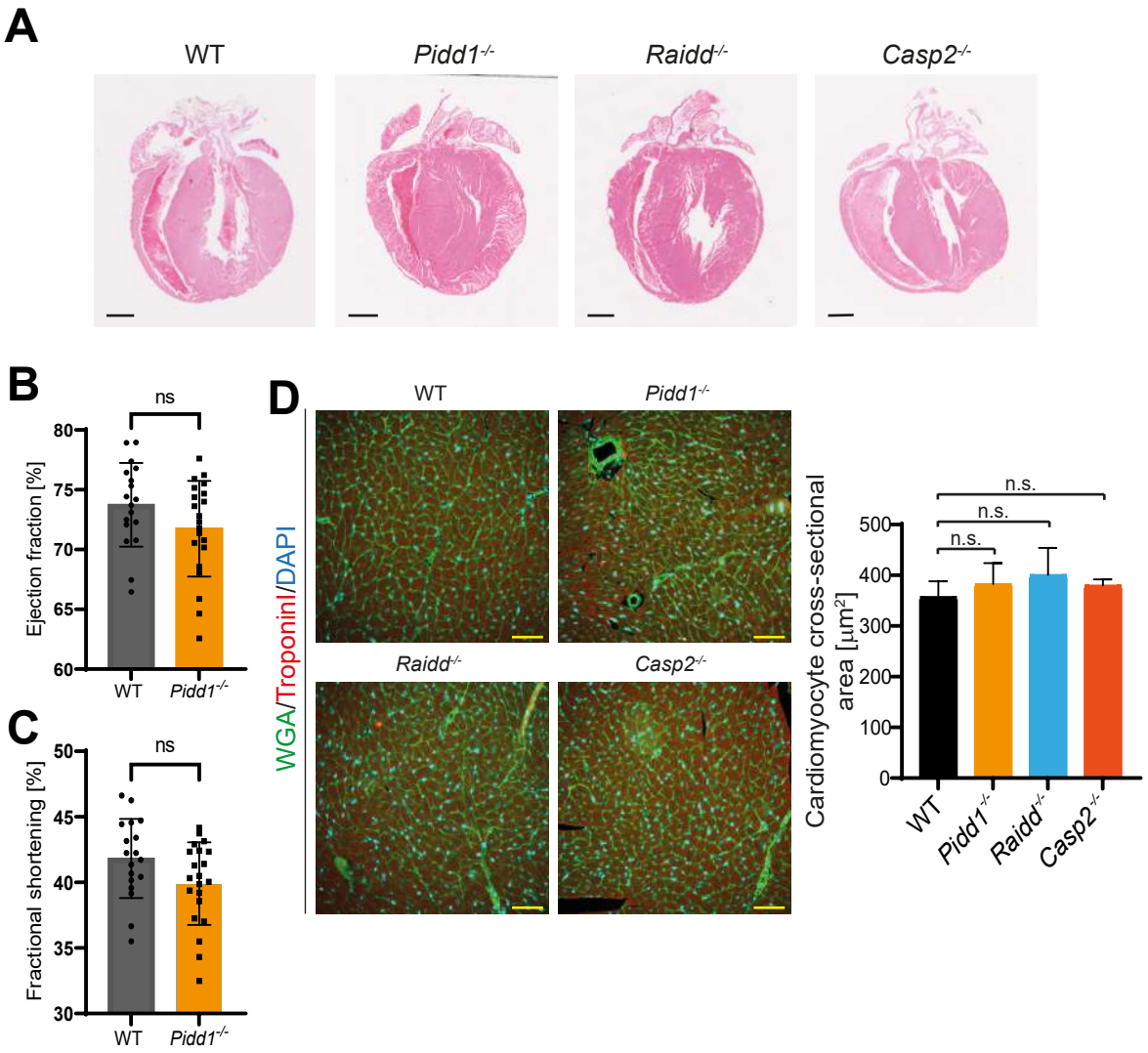

Leone M *et al.* Figure 3

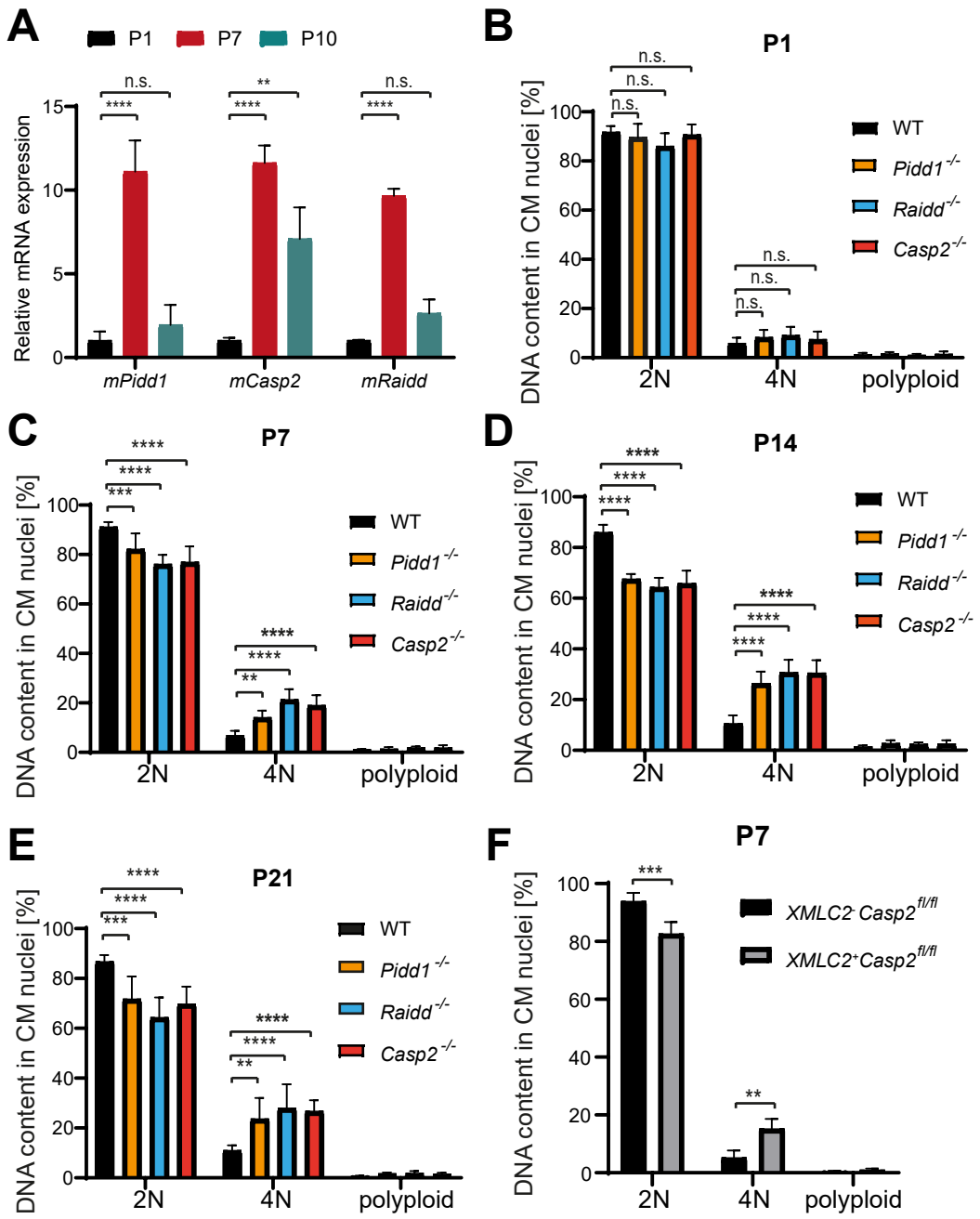
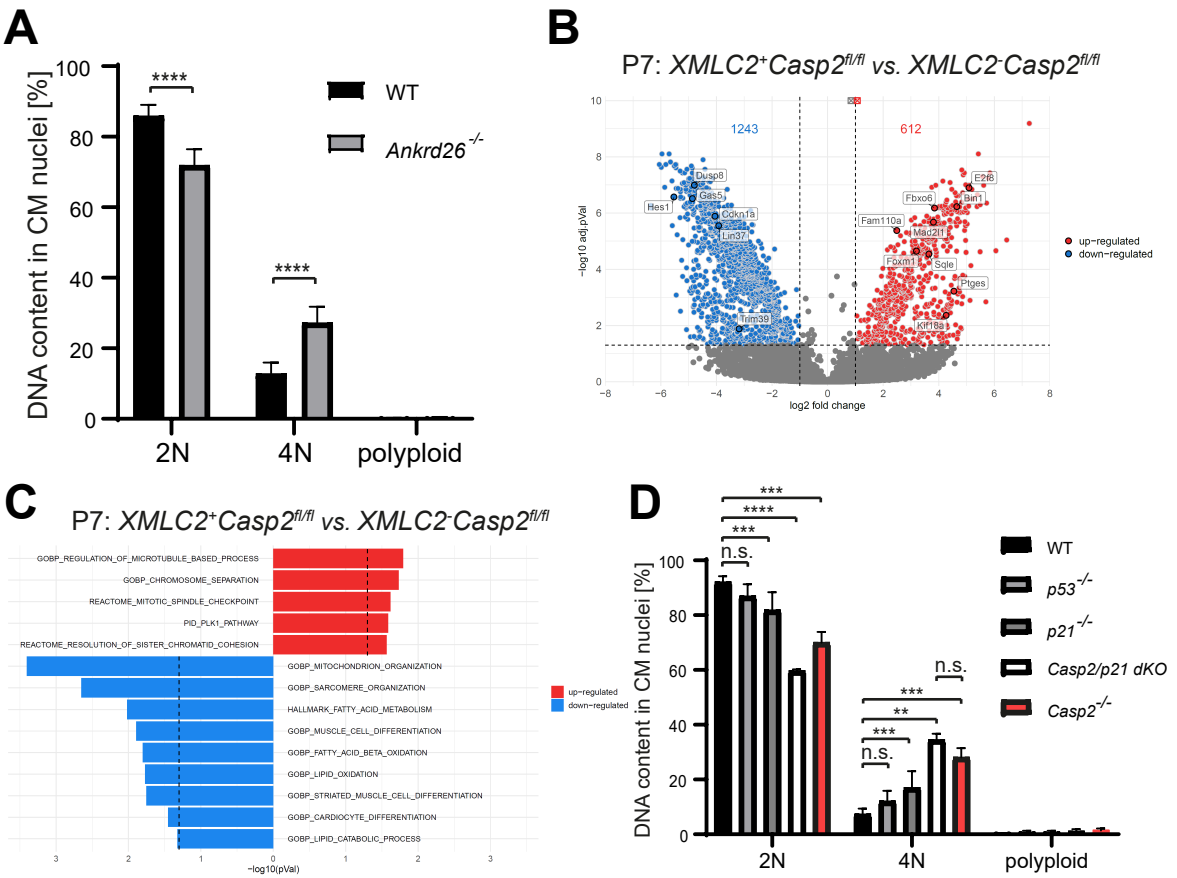
Leone M *et al.* Figure 4